Supplemental Material: Quadrupole spin polarization as signature of second-order topological superconductors

Kirill Plekhanov,[1] Niclas Müller,[2] Yanick Volpez,[1] Dante M. Kennes,[2, 3] Herbert Schoeller,[2] Daniel Loss,[1] and Jelena Klinovaja[1]

[1]*Department of Physics, University of Basel, Klingelbergstrasse 82, CH-4056 Basel, Switzerland*
[2]*Institut für Theorie der Statistischen Physik, RWTH Aachen, 52056 Aachen, Germany and JARA - Fundamentals of Future Information Technology*
[3]*Max Planck Institute for the Structure and Dynamics of Matter and Center for Free-Electron Laser Science, 22761 Hamburg, Germany*

S1. Microscopic details of the models

In this section, we provide microscopic details on the Hamiltonians $\mathcal{H}_0$ and $\mathcal{H}_0'$ considered in the main text of the manuscript. We also describe possible venues for an experimental realization of corresponding physical systems.

Firstly, we consider the Hamiltonian

$$\mathcal{H}_0(\boldsymbol{k}) = 2t\left[2 - \cos(k_x a) - \cos(k_y a)\right]\eta_z - \mu_0\eta_z + \Gamma\eta_z\tau_x$$
$$+ \alpha\left[\sin(k_y a)\sigma_x - \sin(k_x a)\eta_z\sigma_y\right]\tau_z + \Delta_{\mathrm{sc}}\eta_y\sigma_y\tau_z \quad \text{(S1)}$$

from Eq. (1) of the main text. This Hamiltonian was first introduced in Ref. [1], where it was used to describe a system composed of two Rashba layers that are tunnel coupled to each other with an amplitude Γ. Here, t is the term proportional to the kinetic energy of the electrons, which is the same in both layers. Moreover, each layer is assumed to have Rashba spin-orbit interactions with an amplitude α of opposite signs. In what follows, we consider $t, \alpha > 0$. The chemical potential μ_0 is tuned to the spin-orbit crossing point at $\boldsymbol{k} = 0$. Finally, the system is coupled to a 2D s-wave superconducting Josephson junction with a phase factor of π, inducing a superconducting pairing Δ_{sc} via the proximity effect. The Pauli matrices η_j act on the particle-hole space, σ_j – on the spin space, and τ_j – on the space associated with two Rashba layers. The lattice spacing is denoted by a.

Secondly, we consider the Hamiltonian

$$\mathcal{H}_0'(\boldsymbol{k}) = \left\{\Gamma - 2t_x\left[1 - \cos(k_x a)\right] - 2t_y\left[1 - \cos(k_y a)\right]\right\}\eta_z\tau_z$$
$$- \mu_0\eta_z + \left[\alpha_x\sin(k_x a)\sigma_z\tau_x - \alpha_y\sin(k_y a)\eta_z\tau_y\right] + \Delta_{\mathrm{sc}}\eta_y\sigma_y \quad \text{(S2)}$$

from Eq. (5) of the main text. In the regime when $t_x \sim t_y$ and $\alpha_x \sim \alpha_y$, $\mathcal{H}_0'$ can be seen as a modified version of the BHZ Hamiltonian [2], where we neglect the usual kinetic term (which does not have any effect on the topological description), but where we take into account the anisotropy effect in the xy-plane. In this case, the degrees of freedom associated with τ_j correspond to electron/hole orbitals. The hopping amplitudes t_x and t_y describe antisymmetric components of the kinetic term, while α_x and α_y are the spin-orbit interaction amplitudes. In what follows, all these parameters are assumed to be strictly greater than zero. The parameter Γ is responsible for
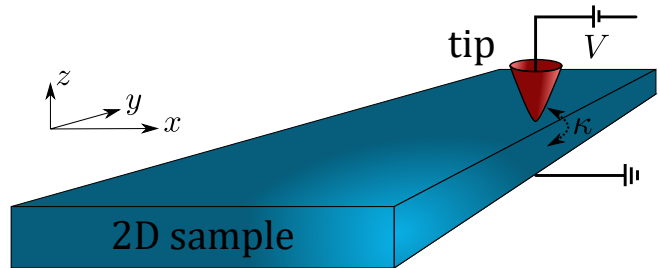

FIG. S1. Schematic representation of the setup. The spin-polarized STM tip biased at voltage V is brought close to the 2D sample which realizes a SOTSC. The current measured using STM allows one to probe the topological phase diagram of the SOTSC.

the topological phase transition between a trivial insulator and the TI. In a quantum well experimental setup, Γ depends on the thickness of the quantum well [3–5].

In addition to the BHZ model, $\mathcal{H}_0'$ can also be generated using a coupled wire construction [6, 7] in a strongly anisotropic regime with $t_y \ll t_x$, $\alpha_y \ll \alpha_x$. In this case, t_x and α_x correspond to the kinetic and Rashba terms along the wire direction, while t_y and α_y correspond to the inter-wire couplings, which are much smaller in amplitude.

S2. Numerical methods

In an STM measurement, the tip of the microscope, biased at the voltage V, is brought close to the sample. This results in a current flowing through the tip into the sample, the amplitude of which depends on the LDOS of the sample and on the overlap between the wavefunctions of the sample and the tip. Hence, if the tip is spin-polarized, the STM measurement will provide additional information on the spin polarization of the sample. Moreover, the voltage difference between the sample and the tip determines how many eigenstates contribute to the current. We note that, alternatively, one can use spin-polarized quantum dots [8–10], however, they are less mobile.

In our work, we model the STM measurement and perform numerical simulations using the Keldysh formal-

ism [11]. To do this calculation, we consider the following setup consisting of two parts: the sample, corresponding to a 2D SOTSC, and the STM tip, are described by the Hamiltonians $\mathcal{H}_{\mathrm{sam}}$ and $\mathcal{H}_{\mathrm{tip}}$, respectively. The STM tip is tunnel coupled to the sample with an amplitude denoted by κ (see Fig. S1). The sample is simulated on a square lattice, and the tunneling between the tip and the sample is assumed to occur locally at one given site of the lattice, depending on the position of the tip. The effect of the applied voltage V induces the difference of the chemical potential eV between the tip and the sample, with e – the electron charge. The influence of the tip is encoded in the induced self-energy which dresses the bare Green's function of the sample. The resulting time-dependent current flowing from the probe reservoir into the sample at time t can be expressed using the Keldysh formalism as

$$J(t) = -e \int \mathrm{d}t' \mathrm{Tr} \left\{ \Sigma^R(t,t')G^<(t',t) - G^<(t,t')\Sigma^A(t',t) \right\},$$
(S3)

where $\Sigma^{\mathrm{R/A}}$ are the retarded/advanced self-energies of the STM tip, $G^{\lessgtr}$ are the fully dressed greater/lesser Green's functions of the sample, and e is the electron charge which is assumed to be equal to one. In the wide band limit and at the equilibrium, the above expression simplifies to

$$J = e\mathrm{Tr} \int \frac{\mathrm{d}\omega}{2\pi} \Sigma^<(\omega)G^R(\omega)\Sigma^<(\omega)G^A(\omega).$$
(S4)

In the main part of the manuscript, we mostly focus on the features of the sample close to the boundary, and show that they provide an alternative way to probe the topological phase transition in some classes of SOTSCs. We also present how the result of such a calculation varies as a function of the tip polarization and the sample Hamiltonian $\mathcal{H}_{\mathrm{sam}}$, describing different types of SOTSCs. In the section "Quadrupolar structure of $\langle S_\perp \rangle$" the sample Hamiltonian is taken to be $\mathcal{H}$, while in the section "Quadrupolar structure of $\langle S_\parallel \rangle$" it is $\mathcal{H}'$.

S3. Analytical calculation of edge states and spin polarization

In this section, we provide details on the analytical calculation of the wavefunctions associated with helical states in both models considered in the main text. We also study the effect of the perturbations, which are added to the models in order to gap out the helical modes, and calculate the expectation values of the spin operators to deduce their spin polarization.

A. SOTSC with two corner states

1. Properties of the $s = 0$ edge

We start with the model described by the Hamiltonian $\mathcal{H}_0$ from Eq. (1) of the main text [1]. We fix the chemical potential as $\mu_0 = 0$ and take the lattice spacing a to be equal to one. First, we consider the $s = 0$ edge localized at $y = 0$. We focus on the physics at the point $k_x = 0$, which describes the solutions uniform along the x axis. We also linearize the resulting problem around the Fermi momenta $k_{\mathrm{F,i}} = 0$ and $k_{\mathrm{F,e}} = \arctan(\alpha/t)$ [12]. In order to do this, we switch to the basis of slowly varying left and right movers

$$\tilde{\psi}_{\uparrow 1} = \tilde{L}_{\uparrow 1}e^{-ik_{\mathrm{F,e}}y} + \tilde{R}_{\uparrow 1}, \quad \tilde{\psi}_{\downarrow 1} = \tilde{L}_{\downarrow 1} + \tilde{R}_{\downarrow 1}e^{ik_{\mathrm{F,e}}y},$$
$$\tilde{\psi}_{\uparrow \bar{1}} = \tilde{L}_{\uparrow \bar{1}} + \tilde{R}_{\uparrow \bar{1}}e^{ik_{\mathrm{F,e}}y}, \quad \tilde{\psi}_{\bar{1}\downarrow} = \tilde{L}_{\bar{1}\downarrow}e^{-ik_{\mathrm{F,e}}y} + \tilde{R}_{\bar{1}\downarrow},$$
(S5)

defined such that $\tilde{\sigma} = \uparrow, \downarrow$ denotes the spin projection onto the x axis. In this new basis, the linearized Hamiltonian reduces to

$$\tilde{\mathcal{H}}_0 = \alpha k_y \delta_z + \Gamma \eta_z \left(\tau_x \delta_x - \tau_y \delta_y \tilde{\sigma}_z \right) \eta_z/2 + \Delta_{\mathrm{sc}} \eta_y \tilde{\sigma}_y \tau_z \delta_x,$$
(S6)

where the Pauli matrices δ_j act on the space of left and right movers. The obtained problem can be solved by substituting $k_y = -i\partial_y$ and imposing vanishing boundary condition at $y = 0$. We find that in the region $\Gamma > \Delta_{\mathrm{sc}}$, the system admits two zero-energy solutions described by the following wavefunctions:

$$\Psi_{0,+}^0(y) = \frac{1}{\mathcal{N}} \left(f_1, g_1, f_1^*, g_1^*, f_{\bar{1}}, g_{\bar{1}}, f_{\bar{1}}^*, g_{\bar{1}}^* \right)^T,$$
$$\Psi_{0,-}^0(y) = \frac{1}{\mathcal{N}} \left(g_1^*, -f_1^*, g_1, -f_1, g_{\bar{1}}^*, -f_{\bar{1}}^*, g_{\bar{1}}, -f_{\bar{1}} \right)^T,$$
(S7)

where we used Eq. (S5) to go back to the original basis $(\psi_{\uparrow 1}, \psi_{\downarrow 1}, \psi_{\uparrow 1}^\dagger, \psi_{\downarrow 1}^\dagger, \psi_{\uparrow \bar{1}}, \psi_{\downarrow \bar{1}}, \psi_{\uparrow \bar{1}}^\dagger, \psi_{\downarrow \bar{1}}^\dagger)$. Here $\mathcal{N}$ is the normalization constant, and the functions f_τ and g_τ are expressed as

$$f_1 = g_{\bar{1}} = -if_{\bar{1}}^* = -ig_1^* = e^{-y/\xi_i} - e^{ik_{\mathrm{F,e}}y}e^{-y/\xi_e}, \quad (S8)$$

with $\xi_i = \alpha/(\Gamma - \Delta_{\mathrm{sc}})$ and $\xi_e = \alpha/\Delta_{\mathrm{sc}}$. As expected from the Kramers partner of gapless helical modes in a helical topological superconductor, the two obtained solutions satisfy $T\left|\Psi_{0,\pm}^0\right\rangle = \pm\left|\Psi_{0,\mp}^0\right\rangle$ and $P\left|\Psi_{0,\pm}^0\right\rangle = \left|\Psi_{0,\pm}^0\right\rangle$, where $P = \eta_x K$ is the particle-hole symmetry operator.

By using the particular form of the solutions at $k_x = 0$, obtained in Eq. (S7), we can now include perturbatively the omitted Zeeman term as well as the first order kinetic term in k_x. To begin with, we express the term linear in k_x as

$$\left\langle \Psi_{0,\pm}^0 \right| -\alpha k_x \eta_z \sigma_y \tau_z \left| \Psi_{0,\pm}^0 \right\rangle = \pm v_{\mathrm{F}} k_x,$$
$$\left\langle \Psi_{0,+}^0 \right| -\alpha k_x \eta_z \sigma_y \tau_z \left| \Psi_{0,-}^0 \right\rangle = 0,$$
(S9)

where $v_{\mathrm{F}} = \alpha\Delta/\Gamma$ is the Fermi velocity of the edge modes. Similarly, the two components of the Zeeman term can be expressed as

$$\left\langle \Psi^0_{0,\pm} \left| \Delta_{\mathrm{z}} \cos(\theta_{\mathrm{z}})\eta_z\sigma_x \right| \Psi^0_{0,\pm} \right\rangle = 0,$$
$$\left\langle \Psi^0_{0,+} \left| \Delta_{\mathrm{z}} \cos(\theta_{\mathrm{z}})\eta_z\sigma_x \right| \Psi^0_{0,-} \right\rangle = i\Delta_{\mathrm{z}} \cos(\theta_{\mathrm{z}}),$$
$$\left\langle \Psi^0_{0,\pm} \left| \Delta_{\mathrm{z}} \sin(\theta_{\mathrm{z}})\sigma_y \right| \Psi^0_{0,\pm} \right\rangle = 0,$$
$$\left\langle \Psi^0_{0,+} \left| \Delta_{\mathrm{z}} \sin(\theta_{\mathrm{z}})\sigma_y \right| \Psi^0_{0,-} \right\rangle = 0. \tag{S10}$$

Combining these two results, we recover the effective Jackiw-Rebbi Hamiltonian

$$\mathcal{H}_{\mathrm{eff},0}(k_x) = v_{\mathrm{F}} k_x \rho_z - \Delta_{\mathrm{z}} \cos(\theta_{\mathrm{z}})\rho_y, \tag{S11}$$

which describes the low-energy physics of the edge $s = 0$.

2. Remaining edges and quadrupolar structure of the spin polarization

Next, we obtain similar results for the three remaining edges of the system by using the rotational symmetry of the Hamiltonian $\mathcal{H}_0$. The rotational symmetry operator can be explicitly written down as $U_{\mathrm{rot}}(\theta) = \exp\left[i\theta\left(L_z + S_z\right)\right]$, where $L_z = -i(x\partial_y - y\partial_x)$ and $S_z = \eta_z\sigma_z/2$ are the z component of the orbital momentum and the spin, respectively. The non-perturbed Hamiltonian satisfies $U_{\mathrm{rot}}(\theta)\mathcal{H}_0(\boldsymbol{k})U_{\mathrm{rot}}^{-1}(\theta) = \mathcal{H}_0(\boldsymbol{k})$. As a consequence, the expression of the states at the three remaining edges can be obtained by using $\left|\Psi^s_{0,\pm}\right\rangle = U_{\mathrm{rot}}(\theta_s)\left|\Psi^0_{0,\pm}\right\rangle$, where $\theta_s = s\pi/2$. The Zeeman term is not invariant under the rotation symmetry transformation:

$$U_{\mathrm{rot}}^{-1}(\theta)\mathcal{H}_{\mathrm{z}}U_{\mathrm{rot}}(\theta) = \Delta_{\mathrm{z}}\left[\cos(\theta - \theta_{\mathrm{z}})\eta_z\sigma_x + \sin(\theta - \theta_{\mathrm{z}})\sigma_y\right]. \tag{S12}$$

Combining this with the results of Eq. (S10), we deduce that the gap opened by the Zeeman term on the edge s can be expressed as $m_s = \Delta_{\mathrm{z}}\cos(\theta_{\mathrm{z}} - \theta_s)$. We note that this gap, indeed, satisfies $m_0 = -m_2$ and $m_1 = -m_3$, as required by the inversion symmetry.

Finally, we calculate the expectation values of the spin operators $S_\parallel = \cos(\theta_z)\eta_z\sigma_x + \sin(\theta_z)\sigma_y$ and $S_\perp = \cos(\theta_z)\sigma_y - \sin(\theta_z)\eta_z\sigma_x$ in the basis of the eigenstates of the effective Hamiltonian $\mathcal{H}_{\mathrm{eff},s}$ at $k_s = 0$. These states diagonalize $\mathcal{H}_{\mathrm{z}}$ and, hence, can be found as $\left|\Phi^s_\pm\right\rangle = (\left|\Psi^s_{0,+}\right\rangle \mp i\left|\Psi^s_{0,-}\right\rangle)/\sqrt{2}$, in correspondence to the eigenvalues $\pm m_s$. By ordering these states according to their eigenvalues, we recover the two states $\left|\Psi^s_\pm\right\rangle$ of the main text corresponding to the eigenvalues $\pm|m_s|$. Trivially, the parallel component of the spin polarization of these states is equal to

$$\left\langle \Psi^s_\pm \left| S_\parallel \right| \Psi^s_\pm \right\rangle = \pm|m_s|/\Delta_{\mathrm{z}} = \pm|\cos(\theta_{\mathrm{z}} - \theta_s)|. \tag{S13}$$

In order to calculate the perpendicular in-plane component of the polarization, we make use of the fact that

$$\left\langle \Phi^s_\pm \left| S_\perp \right| \Phi^s_\pm \right\rangle = \left\langle \Phi^s_\pm \left| U_{\mathrm{rot}}(\pi/2)S_\parallel U_{\mathrm{rot}}^{-1}(\pi/2) \right| \Phi^s_\pm \right\rangle$$
$$= \left\langle \Phi^{s-1}_\pm \left| S_\parallel \right| \Phi^{s-1}_\pm \right\rangle = \pm m_{s-1}/\Delta_{\mathrm{z}}. \tag{S14}$$
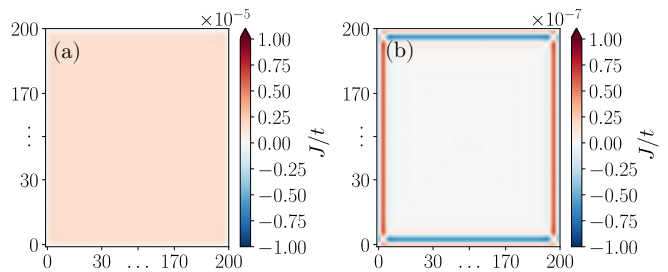

FIG. S2. Numerical calculation of the current J through the spin-polarized STM tip in the topologically trivial phase of $\mathcal{H}$ with $\Gamma = 0.25\Delta_{\mathrm{sc}} = 0.06t$. The polarization of the STM is chosen to be (a) parallel to the Zeeman field and (b) perpendicular to the Zeeman field. The remaining parameters are the same as in Fig. 2 of the main text. The quadrupolar structure of J is absent for the parallel component of the spin polarization. We observe the reminiscence of the quadrupolar structure for the perpendicular component, however the resulting current is several orders of magnitude smaller than in the topological phase (see Fig. 2)

.

Hence, once the states on the s-edge are ordered, we obtain

$$\left\langle \Psi^s_\pm \left| S_\perp \right| \Psi^s_\pm \right\rangle = \pm\mathrm{sgn}(m_s)m_{s-1}/\Delta_{\mathrm{z}}$$
$$= \pm\mathrm{sgn}(m_s)\cos(\theta_{\mathrm{z}} - \theta_{s-1}). \tag{S15}$$

These theoretical arguments are confirmed by numerical simulations of a current flowing through the spin-polarized tip in an STM measurement setup, see Fig. 2 of the main text for a topological phase with $\Gamma = 1.75\Delta_{\mathrm{sc}}$ and Fig. S2 for a topologically trivial phase with $\Gamma = 0.25\Delta_{\mathrm{sc}}$. We find that, in the topological phase, the current is strongest at the edges. When the tip polarization is parallel to the direction of the Zeeman field, the current is approximately uniform and negative along the entire boundary of the systems. However, when the tip polarization is perpendicular to the Zeeman field (but still lying in the xy plane), the current acquires a quadrupolar structure. In the trivial phase, only bulk states contribute to the current and the resulting signal is a few orders of magnitude smaller than in the topological phase.

B. SOTSC with four corner states

1. Properties of the $s = 0$ edge

In the second part of this section, we study the low-energy physics of the model described by the Hamiltonian $\mathcal{H}'_0(\boldsymbol{k})$, see Eq. (5). Similarly to Section S3 A, we start by considering the $s = 0$ edge at $k_x = 0$, corresponding to a uniform solution localized at $y = 0$. We fix $\mu_0 = 0$ and set $a = 1$. Moreover, for a moment, we neglect the superconducting pairing term Δ_{sc}, which we will include later perturbatively. This allows us to focus only on electron or hole parts of the spectrum. To de-

scribe the electron part of the spectrum, we choose the basis $(\psi_{\uparrow 1}, \psi_{\downarrow 1}, \psi_{\uparrow \bar{1}}, \psi_{\downarrow \bar{1}})$. We expand the Hamiltonian up to second order in k_y around $k_y = 0$, which leads us to

$$\mathcal{H}'_0(k_x = 0, k_y) \approx \left(\Gamma - t_y k_y^2\right)\tau_z - \alpha_y k_y \tau_y. \quad (S16)$$

We proceed by substituting $k_y = -i\partial_y$ and looking for zero-energy solutions of the resulting equation. After imposing vanishing boundary condition at $y = 0$, we find two exponentially decaying solutions of the form

$$\Psi'^0_{0,+}(y) = \frac{e^{-y/\xi_+} - e^{-y/\xi_-}}{\mathcal{N}} \left[1, 0, 1, 0\right]^T,$$

$$\Psi'^0_{0,-}(y) = \frac{e^{-y/\xi_+} - e^{-y/\xi_-}}{\mathcal{N}} \left[0, 1, 0, 1\right]^T, \quad (S17)$$

where $\mathcal{N}$ is the normalization constant. Such solutions exist only for $\Gamma > 0$, and the parameters $\xi_\pm$ are given by

$$\xi_\pm^{-1} = \frac{1}{2 t_y}\left(\alpha_y \pm \sqrt{\alpha_y^2 - 4\Gamma t_y}\right). \quad (S18)$$

The two states are related by the time-reversal symmetry such that $T\left|\Psi'^0_{0,\pm}\right\rangle = \pm\left|\Psi'^0_{0,\mp}\right\rangle$. We note that the Hamiltonian defined in Eq. (S16) does not contain Pauli matrices describing the spin space. Hence, the spin quantization axis of the states $\left|\Psi'^0_{0,\pm}\right\rangle$ could be also chosen arbitrarily. Here, we decided to choose the form of the two states as in Eq. (S17), such that it agrees with the choice of the spin quantization axis from the main text and the notation for the edge $s = 1$.

Using the expression of the two states at $k_x = 0$, we calculate the expectation values of the Zeeman term and the kinetic term linear in k_x. For the latter term, we obtain

$$\left\langle \Psi'^0_{0,\pm} \left| \alpha_x k_x \sigma_z \tau_x \right| \Psi'^0_{0,\pm}\right\rangle = \pm v_\mathrm{F} k_x,$$
$$\left\langle \Psi'^0_{0,+} \left| \alpha_x k_x \sigma_z \tau_x \right| \Psi'^0_{0,-}\right\rangle = 0, \quad (S19)$$

where $v_\mathrm{F} = \alpha_x$. The expectation values of the Zeeman term are

$$\left\langle \Psi'^0_{0,\pm} \left| \Delta_\mathrm{z} \sigma_x \right| \Psi'^0_{0,\pm}\right\rangle = 0,$$
$$\left\langle \Psi'^0_{0,+} \left| \Delta_\mathrm{z} \sigma_x \right| \Psi'^0_{0,-}\right\rangle = \Delta_\mathrm{z}. \quad (S20)$$

In order to take into account the superconducting s-wave pairing, we introduce a pair of states $\left|\Psi'^{0*}_{0,\pm}\right\rangle$, which correspond to the particle-hole partners of the states $\left|\Psi'^0_{0,\pm}\right\rangle$. These states belong to the second block of the Nambu space. This allows us to write the effective low-energy Hamiltonian describing the system boundary as

$$\mathcal{H}'_{\mathrm{eff},0}(k_x) = v_\mathrm{F} k_x \rho_z + \Delta_\mathrm{z} \eta_z \rho_x + \Delta_\mathrm{sc} \eta_y \rho_y. \quad (S21)$$

Here, η_j acts in the particle-hole space and ρ_j – in the space of the two edge states. We note that we recover Eq. (7) from the main text with $m_0 = \Delta_\mathrm{z}$. Next, we focus again on the physics at momentum $k_x = 0$ and diagonalize $\mathcal{H}'_{\mathrm{eff},0}$. It is easy to see that the two eigenstates

corresponding to the two lowest magnitude eigenvalues $\pm(\Delta_\mathrm{z} - \Delta_\mathrm{sc})$ can be expressed as

$$\left|\Phi'^0_+\right\rangle = \frac{1}{2}\left(\left|\Psi'^0_{0,+}\right\rangle + \left|\Psi'^0_{0,-}\right\rangle - \left|\Psi'^{0*}_{0,+}\right\rangle + \left|\Psi'^{0*}_{0,-}\right\rangle\right),$$

$$\left|\Phi'^0_-\right\rangle = \frac{1}{2}\left(\left|\Psi'^0_{0,+}\right\rangle - \left|\Psi'^0_{0,-}\right\rangle - \left|\Psi'^{0*}_{0,+}\right\rangle - \left|\Psi'^{0*}_{0,-}\right\rangle\right). \quad (S22)$$

From this, we deduce that

$$\left\langle \Phi'^0_\pm \left| S_\parallel \right| \Phi'^0_\pm\right\rangle = \pm 1, \quad \left\langle \Phi'^0_\pm \left| S_\perp \right| \Phi'^0_\pm\right\rangle = 0, \quad (S23)$$

where $S_\parallel = \eta_z \sigma_x$ and $S_\perp = \sigma_y$ are the parallel and perpendicular components of the spin polarization, respectively. Finally, we sort the states according to their energies, from negative to positive, to arrive at $\left|\Psi'^0_\pm\right\rangle$. The initial ordering of the states $\left|\Phi'^0_\pm\right\rangle$ is correct in the regime $\Delta_\mathrm{z} > \Delta_\mathrm{sc}$, but has to be changed when $\Delta_\mathrm{z} < \Delta_\mathrm{sc}$. Hence, we deduce that in the basis of new, correctly ordered states, the expectation values of the spin polarization become equal to $\left\langle \Psi'^0_\pm \left| S_\parallel \right| \Psi'^0_\pm\right\rangle = \pm 1$ when $\Delta_\mathrm{z} > \Delta_\mathrm{sc}$ and $\left\langle \Psi'^0_\pm \left| S_\parallel \right| \Psi'^0_\pm\right\rangle = \mp 1$ otherwise.

2. Properties of the $s = 1$ edge

In the same way as for the edge $s = 0$, we do the calculations on the second non-equivalent edge of the system denoted by $s = 1$ by considering the physics at $k_y = 0$. After expanding the Hamiltonian $\mathcal{H}'_0(\mathbf{k})$ [see Eq. (5) from the main text] to second order in k_x, we obtain

$$\mathcal{H}'_0(k_x, k_y = 0) \approx \left(\Gamma - t_x k_x^2\right)\tau_z + \alpha_x k_x \sigma_z \tau_x. \quad (S24)$$

By substituting $k_x = -i\partial_x$ and imposing vanishing boundary condition at $x = 0$, we find two exponentially decaying solutions at zero energy which have the form

$$\Psi'^1_{0,+}(x) = \frac{e^{-x/\xi_+} - e^{-x/\xi_-}}{\mathcal{N}} \left[1, 0, i, 0\right]^T,$$

$$\Psi'^1_{0,-}(x) = \frac{e^{-x/\xi_+} - e^{-x/\xi_-}}{\mathcal{N}} \left[0, 1, 0, -i\right]^T, \quad (S25)$$

where the parameters $\xi_\pm$ are given by

$$\xi_\pm^{-1} = \frac{1}{2 t_x}\left(\alpha_x \pm \sqrt{\alpha_x^2 - 4\Gamma t_x}\right). \quad (S26)$$

Similarly, we find that the kinetic term is diagonal in the basis of the two states, with

$$\left\langle \Psi'^1_{0,\pm} \left| \alpha_y k_y \tau_y \right| \Psi'^1_{0,\pm}\right\rangle = \pm v_\mathrm{F} k_y,$$
$$\left\langle \Psi'^1_{0,+} \left| \alpha_y k_y \tau_y \right| \Psi'^1_{0,-}\right\rangle = 0, \quad (S27)$$

where $v_\mathrm{F} = \alpha_y$. However, unlike on the edge $s = 0$, here we find that all expectation values of the Zeeman term are exactly zero

$$\left\langle \Psi'^1_{0,\pm} \left| \Delta_\mathrm{z} \sigma_x \right| \Psi'^1_{0,\pm}\right\rangle = 0,$$
$$\left\langle \Psi'^1_{0,+} \left| \Delta_\mathrm{z} \sigma_x \right| \Psi'^1_{0,-}\right\rangle = 0. \quad (S28)$$

We note that this feature is independent of the orientation of the Zeeman field and is crucial to generate four corner states. Taking into account the proximity induced superconductivity effect, we can now express the effective low-energy Hamiltonian as

$$\mathcal{H}'_{\mathrm{eff},1}(k_y) = v_{\mathrm{F}} k_y \rho_z + \Delta_{\mathrm{sc}} \eta_y \rho_y, \qquad (\text{S29})$$

which we immediately identify with the topologically

trivial regime.

In order to find the spin polarization of the edge states along the edge $s = 1$, we solve the problem by explicitly taking into account the kinetic and Zeeman terms. The new problem is described by the Hamiltonian $\mathcal{H}'_0(k_x, k_y) + \Delta_{\mathrm{z}} \sigma_x$. To lowest order in k_y and Δ_{z}, the corresponding solutions can be expressed as

$$\tilde{\Psi}'^1_{0,+}(x) = \sum_{\lambda=\pm} \lambda \frac{e^{-x/\xi_{1,\lambda}}}{\mathcal{N}} \left[1 + f_{1,\lambda}, 1 + f_{1,\lambda}, i(1 - f_{1,\lambda}), i(f_{1,\lambda} - 1) \right]^T$$
$$+ \sum_{\lambda=\pm} \lambda \frac{e^{-x/\xi_{2,\lambda}}}{\mathcal{N}} \left[1 + f_{2,\lambda}, -(1 + f_{2,\lambda}), i(1 - f_{2,\lambda}), i(1 - f_{2,\lambda}) \right]^T,$$

$$\tilde{\Psi}'^1_{0,-}(x) = \sum_{\lambda=\pm} \lambda \frac{e^{-x/\xi_{1,\lambda}}}{\mathcal{N}} \left[1 + f_{1,\lambda}, 1 + f_{1,\lambda}, i(1 - f_{1,\lambda}), i(f_{1,\lambda} - 1) \right]^T$$
$$- \sum_{\lambda=\pm} \lambda \frac{e^{-x/\xi_{2,\lambda}}}{\mathcal{N}} \left[1 + f_{2,\lambda}, -(1 + f_{2,\lambda}), i(1 - f_{2,\lambda}), i(1 - f_{2,\lambda}) \right]^T,$$

$$(\text{S30})$$

with $f_{j,\pm} = (-1)^j \xi_{j,\pm} \alpha_y k_y / (2\alpha_x)$, $\tilde{\xi}^{-1}_{1,\pm} = \left(\alpha_x \pm \sqrt{\alpha_x^2 - 4(\Gamma + \Delta_{\mathrm{z}}) t_x} \right) / (2t_x)$, and $\tilde{\xi}^{-1}_{2,\pm} = \left(\alpha_x \pm \sqrt{\alpha_x^2 - 4(\Gamma - \Delta_{\mathrm{z}}) t_x} \right) / (2t_x)$. We verify that the new solutions reproduce correctly Eq. (S25) in the limit $\Delta_{\mathrm{z}} = 0$ and $k_y = 0$. We also find that under the

effect of the Zeeman field, the condition of the existence of the edge modes is modified to $\Gamma > |\Delta_{\mathrm{z}}|$, such that the topological phase becomes smaller when the Zeeman field increases. Moreover, the polarization of the edge states is defined by the following expression:

$$\left\langle \tilde{\Psi}'^1_{0,\pm} \left| S_\parallel \right| \tilde{\Psi}'^1_{0,\pm} \right\rangle = \pm 4 \frac{\sum_j \mathfrak{Re} \left[f_{j,+} \xi_{j,+} + f_{j,-} \xi_{j,-} - 4 f_{j,+} f_{j,-} / (\xi^{-1}_{j,+} + \xi^{-1*}_{j,-}) \right]}{\sum_j \mathfrak{Re} \left[\xi_{j,+} + \xi_{j,-} - 4 / (\xi^{-1}_{j,+} + \xi^{-1*}_{j,-}) \right]}. \qquad (\text{S31})$$

As expected, the parallel component of the spin polarization is zero for $\Delta_{\mathrm{z}} = 0$ independently of the value of k_y. The same is true for $k_y = 0$, independently of the value of Δ_{z}. These features are confirmed numerically in Fig. S3(a), where we calculate the spin polarization of the eigenstates of $\mathcal{H}'$ in a geometry with the OBC (PBC) along the x (y) axis as a function of the momentum k_y. Moreover, we find that the spin polarization changes smoothly as a function of Δ_{z}. We also note that both perpendicular components of the spin polarization are exactly zero.

If the superconducting term is taken into account, the spectrum of states $\left| \Psi'^1_{0,\pm} \right\rangle$ acquires a finite gap. Nevertheless, we expect that the spin polarization of the edge states keeps the same sign for different values of the ratio

$\Delta_{\mathrm{z}}/\Delta_{\mathrm{sc}}$ across the entire phase transition. This is confirmed by numerical calculations presented in Fig. S3(b). We also note that for $\Delta_{\mathrm{sc}} \neq 0$, the edge states become spin polarized even at $k_y = 0$.

3. Quadrupolar structure of the spin polarization

Finally, by considering the effect of the inversion symmetry that maps $\boldsymbol{k}$ to $-\boldsymbol{k}$, we relate the description of the edge $s = 2$ ($s = 3$) to the one of the edge $s = 0$ ($s = 1$). More specifically, we use that $I\mathcal{H}'(\boldsymbol{k})I^{-1} = \mathcal{H}'(-\boldsymbol{k})$, where $I = \tau_z$, which implies that the mass terms at opposite edges have opposite signs: $m_0 = -m_2 = \Delta_{\mathrm{z}}$ and $m_1 = -m_3 = 0$. This
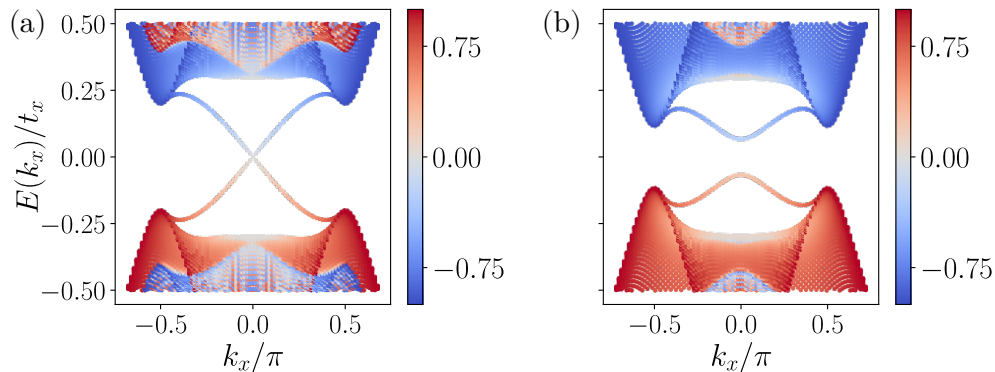
FIG. S3. Numerical calculation of the spin polarization of the eigenstates of $\mathcal{H}'$ in a geometry with OBC (PBC) along the x (y) axis. The color corresponds to $\langle \Psi_j(k_y) | S_\parallel | \Psi_j(k_y) \rangle$, where $|\Psi_j(k_y)\rangle$ is the j-th eigenstate of $\mathcal{H}'$. (a) When $\Delta_{sc} = 0$, the edge spectrum remains gapless and the spin polarization of the states is zero at $k_y = 0$. (b) When $\Delta_{sc} = 0.1t_x$, the edge spectrum is gapped out and the spin polarization becomes non-zero even at $k_y = 0$. Nevertheless, the sign of the spin polarization remains the same as in (a). All the remaining parameters are the same as in Fig. 3(b).
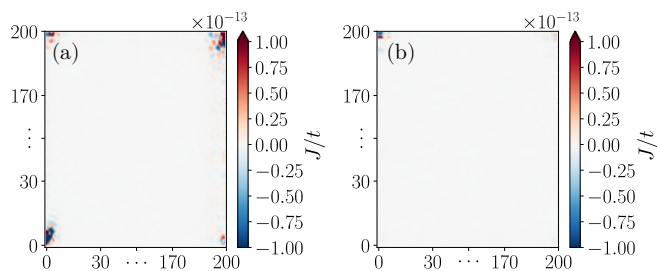
FIG. S4. Numerical calculation of the current J through the STM tip that is polarized perpendicularly to the Zeeman field along the y axis (a) in the topological phase with $\Delta_z = 1.75\Delta_{sc}$ and (b) in the trivial phase with $\Delta_z = 0.25\Delta_{sc}$. The remaining parameters of the simulations are the same as in Fig. 4. The perpendicular component of the spin polarization is trivially zero everywhere except at the four corners of the system.

allows us to see that the total boundary of the system is composed of two pairs of effective Rashba wires forming an alternating pattern, only one of which is affected by the Zeeman field. As a result, in the topological regime $\Delta_z > \Delta_{sc}$, the system is described by the parallel component of the spin polarization flipping its sign from one edge to another, resulting in a quadrupolar spin structure, which can indeed be observed in Fig. 4 of the main text. Such a feature is directly associated with the emergence of MCSs and allows one to probe the topological phase transition which occurs in the system. We also verify numerically (see Fig. S4) that the perpendicular components of the spin polarization are trivially zero everywhere except at the four corners of the system, where they acquire some finite value as a result of the broken translation symmetry along the edge.

S4. Quadrupolar moment

In the main text, we demonstrated that the structure of the edge spin polarization allows one to detect the topological phase transition in SOTSCs with broken time-reversal symmetry. In particular, we found that in SOTSCs hosting a pair of MCSs at two opposite corners the sign of the spin polarization perpendicular to the Zeeman field of low-energy states changes on every edge. This feature has been denoted as quadrupolar structure of the spin polarization. Similarly, we observed that a SOTSC which hosts a MCS at each of the four corners is described by a quadrupolar structure of the spin polarization parallel to the applied Zeeman field.

Here, we further analyze the quadrupolar structure of the spin polarization by introducing the energy-resolved quadrupolar tensor $Q_{\mu\nu}$ associated with the STM current J. Assuming that the sample is a perfect square and by placing the origin of coordinates in the square center we can define the following quantity:

$$Q_{\mu\nu}(E) = \sum_i \left[2r_\mu(i)r_\nu(i) - \mathbb{I}_{\mu\nu}\right] J(\boldsymbol{r}_i, E)/N. \quad \text{(S32)}$$

Here $r_\mu(i)$ denotes the position of the site with the lattice index i and $\mathbb{I}$ is the 2×2 identity matrix. The sum over i runs over all the sites of the system and N denotes the total number of sites. The current $J(\boldsymbol{r}_i, E)$ refers to the contribution defined in Eq. (S4) for a small window $[E - \Delta E/2, E + \Delta E/2]$. We note here that the spin polarization of MCSs [13] does not play a role here as we focus on the signal to be detected away from the corners. We calculate this quantity in both models across the phase transition. We also focus only on the diagonal component $Q_{xx} = -Q_{yy}$ of the quadrupolar tensor with the off-diagonal components being trivially zero.

First, we consider the model presented in Section "SOTSCs with two corner states" [see Fig. S5(a)]. We assume that the STM tip polarization is perpendicular
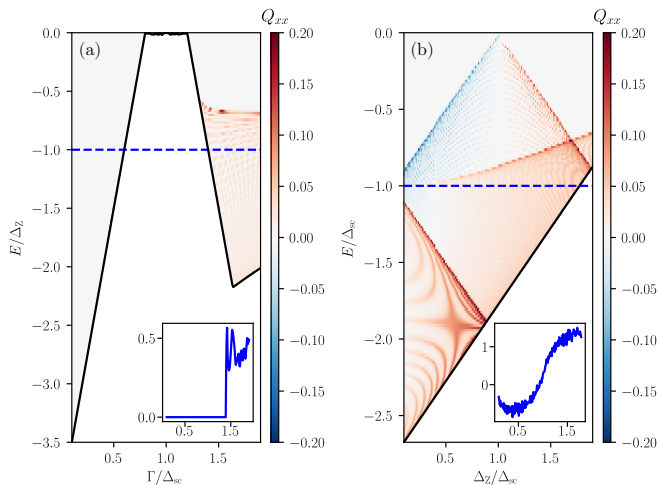
FIG. S5. Energy-resolved value of the quadrupolar moment Q_{xx} evaluated across the topological phase transition for the two models considered in the main text. Insets show the contribution summed from the blue lines up to the chemical potential. Black lines separate the contribution coming from the edges (shown) and the bulk (not shown). (a) The model is described by the Hamiltonian $\mathcal{H}$ and Q_{xx} is calculated as a function of Γ/Δ_{sc} with $\Delta E = 0.02\Delta_z$. All the remaining parameters are the same as in Fig. 2. The trivial (topological) phase corresponds to zero (finite) value of the quadrupolar moment. (b) The model is described by the Hamiltonian $\mathcal{H}'$ and Q_{xx} is calculated as a function of Δ_z/Δ_{sc} with $\Delta E = 0.015\Delta_{sc}$. All the remaining parameters are the same as in Fig. 4. The spin polarization of the x-edge states changes sign at the phase transition, while for y-edge states it slowly increases with Δ_z. As a consequence, the integrated value of Q_{xx} crosses zero close to the topological phase transition point.

to the Zeeman field and calculate Q_{xx} as a function of Γ/Δ_{sc}. We find that in the topologically trivial phase, the quadrupolar moment is exactly zero, since no available edge states are present in the considered energy window. In the topological phase, on the contrary, Q_{xx} is positive that can be associated with the quadrupolar structure of spin polarization at the edges.

Similarly, we consider the model presented in Section "SOTSCs with four corner states" with the STM tip polarization being parallel to the Zeeman field [see Fig. S5(b)]. We clearly distinguish the contribution coming from different edges: the energy of the x-edge states increases with Δ_z until it reaches zero at the critical point $\Delta_z = \Delta_{sc}$, after which it starts decreasing again; a large quadrupolar moment flips sign at the phase transition. For $\Delta_z > \Delta_{sc}$, we also observe the emergence of edge states at lower energies, which live on the x-edge and are described by the spin polarization of an opposite sign. At the same time, the energy of the y-edge states as well as their quadrupolar moment slowly increases with Δ_z without flipping its sign. As a result, when integrated over the energy E, the quadrupolar moment changes sign at the topological phase transition.
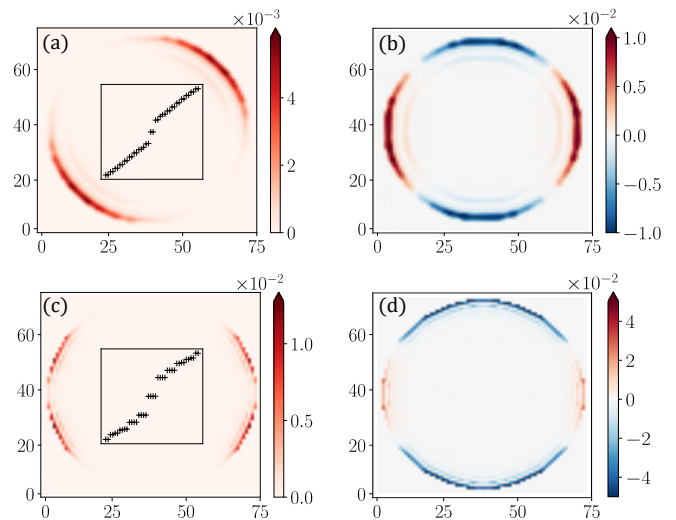

FIG. S6. (a) Numerical calculation of the MCS wavefunctions and (b) the total spin polarization of 40 states below the Fermi level in the topological phase of the system described by the Hamiltonian $\mathcal{H}$ in a disk geometry. The parameters used are $\Gamma = 2\Delta_{sc} = \alpha = 0.5t$, $\mu_0 = 0$, $\Delta_z = 0.05t$, and $\theta_z = \pi/4$. (c,d) The same calculation as before but the system is now described by the Hamiltonian $\mathcal{H}'$ with $\Gamma = t_y = t_x$, $\alpha_x = \alpha_y = 0.3t_x$, $\mu_0 = 0$, and $\Delta_z = 2\Delta_{sc} = 0.1t_x$. As expected, in both cases, we observe MCSs, emphasizing that the shape of the sample does not play a substantial role. The corresponding spin polarization shows the quadrupole structure.

We notice that the precise value of Q_{xx} depends strongly on the energy E. Nevertheless, the quadrupolar structure, namely the sign change of the spin polarization on the neighboring edges of the system, is typical for topological phases close to the phase boundary. Hence, the quadrupolar structure of the spin polarization remains a prominent probe of the SOTSCs topology as long as the effective low-energy description stays valid.

Finally, we note that the quadrupolar tensor $Q_{\mu\nu}(E)$ is less suitable for direct experimental observation as it requires integration of the current signal across the entire sample. Moreover, the values of $Q_{\mu\nu}(E)$ depend on the sample geometry such as size and shape, as well as on the choice of coordinate origin in the definition of $Q_{\mu\nu}$, since, in general, the total spin polarization and dipole moments are non-zero.

S5. Stability of quadrupolar polarization

We also provide additional numerical results, demonstrating the stability of the quadrupolar polarization feature for the two SOTSC classes considered in the main text. To do this, we simulate the system in a disc geometry, which does not have any well defined edges and corners. Nevertheless, MCSs still emerge in such a geometry. Their position is unambiguously determined by the symmetries of the system, namely, the inversion symme-
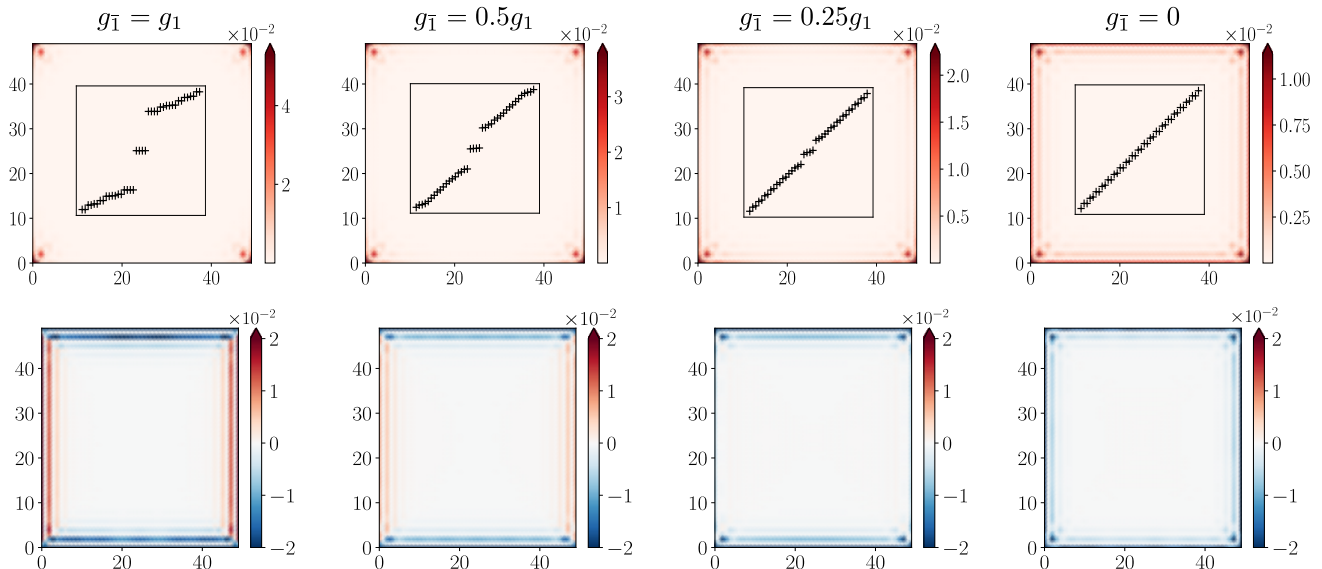
FIG. S7. (first row) Numerical calculation of the MCS wavefunctions and (second row) the total spin polarization of 40 states below the Fermi level in the topological phase of a system described by the Hamiltonian $\mathcal{H}'$ for different values of the g-factor ratio $g_{\bar{1}}/g_1$ (different columns). The remaining parameters are the same as in Fig. 3(b) of the main text. We confirm that the inversion symmetry between two bands, which gets broken if g-factors are different, is indeed not needed. The MCSs survive even if the g-factors are substantially different.

try I of the Hamiltonian $\mathcal{H}$ from the section "SOTSCs with two corner states" and the in-plane anisotropy of the Hamiltonian $\mathcal{H}'$ from the section "SOTSCs with four corner states" of the main text. In Figs. S6(a) and (b), we show that, in the model described by $\mathcal{H}$, two corner states emerge at two opposite extremities of the disc, aligned with the direction of the Zeeman field. The perpendicular component of the spin polarization changes sign at four equal-sized quadrants delimited by the Zeeman field vector and the vector normal to it. Similarly, in Figs. S6(c) and (d), we show that four corner states emerge in the model described by $\mathcal{H}'$, dividing the disk into four quadrants. The parallel component of the spin polarization has opposite signs in neighboring quadrants, while the perpendicular component remains trivially zero everywhere. The size of the quadrants is determined by the ratio Δ_z/Δ_{sc}, such that in the limit $\Delta_z \ll \Delta_{sc}$ the

corner states merge pairwise at the top and bottom extremities of the disk.

Additionally, having in mind an experimental realization in quantum wells [3–5, 14–17] of our model with four corner states described by the Hamiltonian $\mathcal{H}'$, we study how the topological phase diagram and the result of the STM measurement vary as a function of g-factors of the electron and hole bands, denoted by g_1 and $g_{\bar{1}}$, respectively. The result of such a calculation is presented in Fig. S7. We find that the topological phase and, as a result, the quadrupolar polarization feature are stable even for a strong g-factor anisotropy. However, when $g_{\bar{1}}$ becomes of the order of $0.25g_1$ (and vice versa), a phase transition occurs leading to the closing of the bulk gap, accompanied by the disappearance of the corner states as well as of the quadrupolar structure of the spin polarization.

[1] Y. Volpez, D. Loss, and J. Klinovaja, Phys. Rev. Lett. **122**, 126402 (2019).

[2] B. A. Bernevig, T. L. Hughes, and S. Zhang, Science **314**, 5806 (2006).

[3] M. König, S. Wiedmann, C. Brüne, A. Roth, H. Buhmann, L. W. Molenkamp, X. Qi, S. Zhang, Science **318**, 766 (2007).

[4] A. Roth, C. Brüne, H. Buhmann, L. W. Molenkamp, J. Maciejko, X. L. Qi, and S. C. Zhang, Science **325**, 294 (2009).

[5] C. Liu, T. L. Hughes, X. L. Qi, K. Wang, and S. C. Zhang, Phys. Rev. Lett. **100**, 236601 (2008).

[6] C. L. Kane, R. Mukhopadhyay, and T. C. Lubensky, Phys. Rev. Lett. **88**, 036401 (2002).

[7] J. C. Y. Teo and C. L. Kane, Phys. Rev. B **89**, 085101 (2014).

[8] D. Chevallier, P. Szumniak, S.Hoffman, D. Loss, and J. Klinovaja, Phys. Rev. B **97**, 045404 (2018).

[9] D. Chevallier and J Klinovaja, Phys. Rev. B **94**, 035417 (2016).

[10] M. M. Maska and T. Domanski, Scientific Reports **7**, 16193 (2017).

[11] N. Müller, D. M. Kennes, J. Klinovaja, D. Loss, and H. Schoeller, Phys. Rev. B **101**, 155417 (2020).

[12] J. Klinovaja and D. Loss, Phys. Rev. B **86**, 085408 (2012).

[13] D. Sticlet, C. Bena, and P. Simon, Phys. Rev. Lett. **108**, 096802 (2012).

[14] S. B. Zhang, Y. Y. Zhang, and S. Q. Shen, Phys. Rev. B **90**, 115305 (2014).

[15] R. Skolasinski, D. I. Pikulin, J. Alicea, and M. Wimmer, Phys. Rev. B **98**, 201404(R) (2018).

[16] C. Li, S. Zhang, and S. Shen, Phys. Rev. B **97**, 045420 (2018).

[17] F. Schulz, K. Plekhanov, D. Loss, and J. Klinovaja, arXiv:2004.10623.